Materials & Design 253 (2025) 113873

Contents lists available at ScienceDirect

Materials & Design

journal homepage: www.elsevier.com/locate/matdes

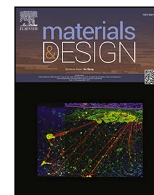

Quantifying delamination energy in tungsten on silicon thin films through nanoindentation and nanoscratch

Shatha Almarri *, Matthew Lloyd, Ed Darnbrough, David Armstrong

Department of Materials, University of Oxford, Oxford OX1 3PH, UK

ARTICLE INFO

Keywords:
Tungsten
Nanoindentation
Nanoscratch
Adhesion
Thin film

ABSTRACT

Quantifying delamination energy is crucial for the reliability and longevity of thin films. In this work, the delamination energy in tungsten-silicon thin films is investigated through nanoindentation and nanoscratching. Nanoindentation was also employed to assess the mechanical properties of the coating through the use of substrate corrections. Energy methods were used to analyse the nanoindentation load displacement curves to quantify the delamination energy. Finite element modelling was used to further improve the accuracy of the calculated delamination energy. Nanoscratching was found to be highly sensitive to the scratch parameters used, and the effect of scratch parameters on the critical load and delamination energy was investigated. It was found that the presence of fragmentation event in nanoscratching led to higher delamination energy values as compared to nanoindentation. Nanoindentation was found to output values closer to that of literature and were additionally not parameter sensitive, making it a reliable method of evaluating thin film adhesion.

1. Introduction

Thin films have emerged as an important class of materials with applications in a wide range of industries such as semiconductors[1], coatings[2], energy storage[3,4], medical devices[5], and photovoltaics [6]. In many of these applications, these thin films experience mechanical stress due to external forces or internal strains[7,8]. The efficiency of stress transfer in thin films depends on how well the film is adhered to the substrate, therefore the overall strength of the thin film greatly depends on the interfacial strength between the film and substrate.

Fundamental adhesion is a very difficult property to measure directly [9]. The thermodynamic adhesion at a dissimilar interface is defined as the energy that must be overcome to convert that interface into two free surfaces and is related to the *in-vacuo* surface free energies of the film (γ_F), the substrate (γ_S), and the specific free energy of the contact interface in equilibrium (γ_{FS}) as follows[10] (Eq. (1)):

$$W_{FS} = \gamma_F + \gamma_S - \gamma_{FS} \tag{1}$$

It is difficult to measure these values directly, leading researchers to measure the practical or experimental adhesion. Experimental adhesion only provides a measure of the extrinsic value of the adhesive strength, which depends on the type of test being conducted, and is not a quantitative value of the fundamental adhesion in the system[9,10]. Conventional methods to measure adhesion of thin films include semi-quantitative peel[11] and micro-scratch tests[12–14]. Complex and time-consuming methods have been developed for specific applications such as micro-cantilever bending[15,16], but these are not applicable to all situations.

Marshall and Evans[17] pioneered the use of nanoindentation for characterising adhesive strengths by providing a linear fracture mechanics approach to the solution of the energy release rate as a function of the residual and applied stresses during indentation. The indentation volume (V_0) required to calculate the energy release rate is defined in Eq. (2) as:

$$V_0 = \frac{\pi}{3} h_P^3 tan\varphi^2 \tag{2}$$

Where h_P is the plastic indentation depth, and φ is the indenter cone angle.

An assumption of this method is that the indentation volume remains within the film through-out the delamination test. This assumes that there is no pile-up around the indent forms nor is there any substrate deformation occurring under the indent. This model is therefore not applicable in ductile films that display pile-up behaviour, and calculating the indentation volume incorrectly can lead to large variations in

* Corresponding author.
E-mail address: shatha.almarri@materials.ox.ac.uk (S. Almarri).

https://doi.org/10.1016/j.matdes.2025.113873
Received 13 November 2024; Received in revised form 5 March 2025; Accepted 22 March 2025
Available online 25 March 2025
0264-1275/© 2025 The Authors. Published by Elsevier Ltd. This is an open access article under the CC BY license (http://creativecommons.org/licenses/by/4.0/).

Table 1
Parameters that affect the critical load during scratch test.

Intrinsic Parameters	Extrinsic Parameters
Coating thickness	Scratch loading rate
Coating hardness	Scratch displacement rate
Substrate hardness	Indenter shape
	Intender tip radius

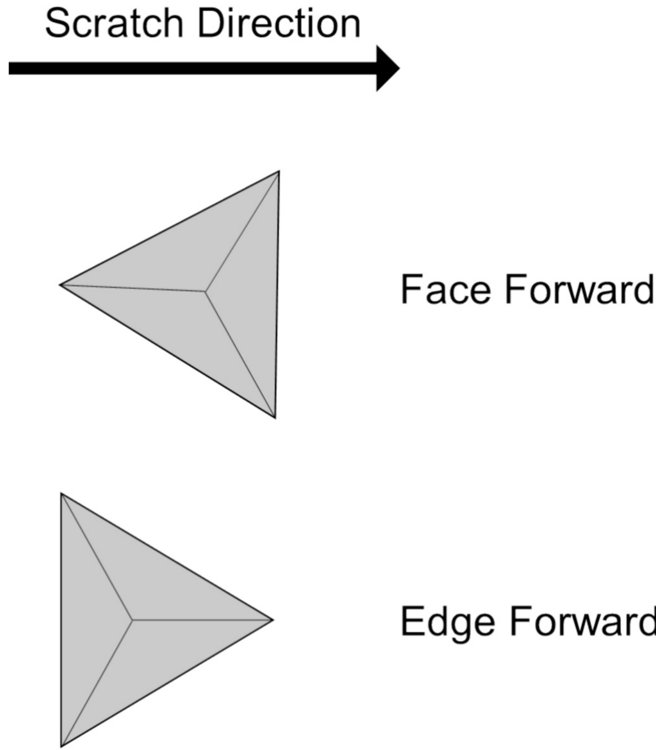

Fig. 1. Face forward and edge forward orientations of a Berkovich tip.

delamination energy[18]. Other researchers have shown that the delamination work done by the indenter can be calculated by analysing the areas under the nanoindentation load–displacement curves, which allows for a simpler energy consideration of adhesion. This has previously been done in the literature to measure delamination and fracture energies in ductile[19–21] and brittle[22–24] films.

The critical load to cause coating failure during a scratch test is a qualitative measure of adhesion[25]. Laugier[26] developed a semi-quantitative test that converts scratch critical loads into values of adhesive energy. The measured critical load during scratch testing is sensitive to a number of intrinsic and extrinsic parameters, summarized in Table 1. Therefore, scratch testing is not used as a quantitative measure of adhesion and is used for comparative studies[27–30].

The literature comparing nanoindentation and nanoscratching delamination energies is extremely limited in number[31,32]. The objective of this paper is to understand the delamination deformation mechanisms that occur during nanoindentation and nanoscratching tests, and to compare the values of delamination energy results from both tests. Parametric studies have been conducted to further understand the effect on measured delamination energy. Finally, finite element modelling has been used to improve on existing nanoindentation delamination methods.

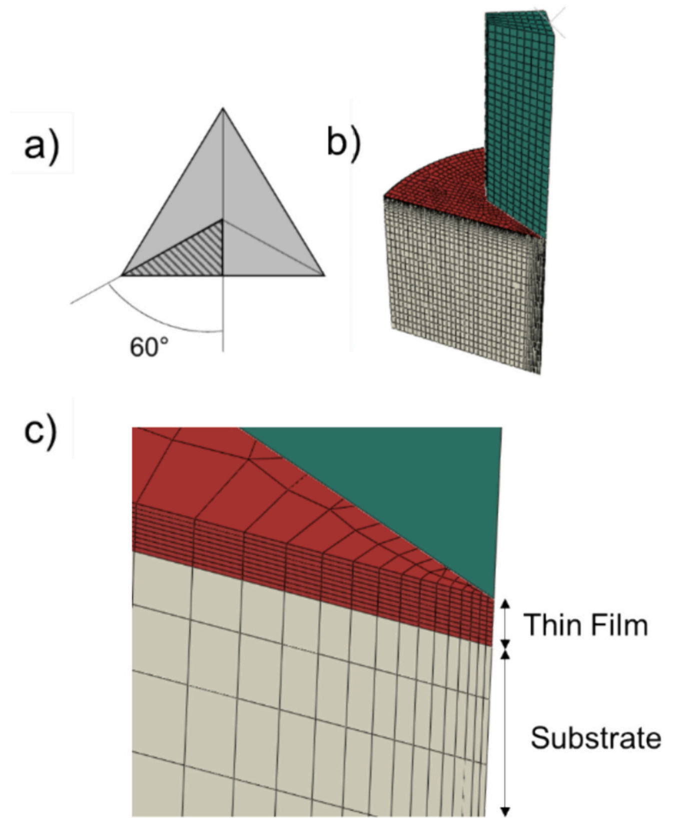

Fig. 2. a) the shaded region shows the symmetry axes used. b) and c) show the 3d geometry of model used where the indenter is denoted in green, thin film in red, and substrate in grey.

Table 2
FEA model Materials Properties.

	Young's Modulus (GPa)	Poisson Ratio	Yield Strength (MPa)
Tungsten	410	0.28	750
Silicon	194	0.3	–

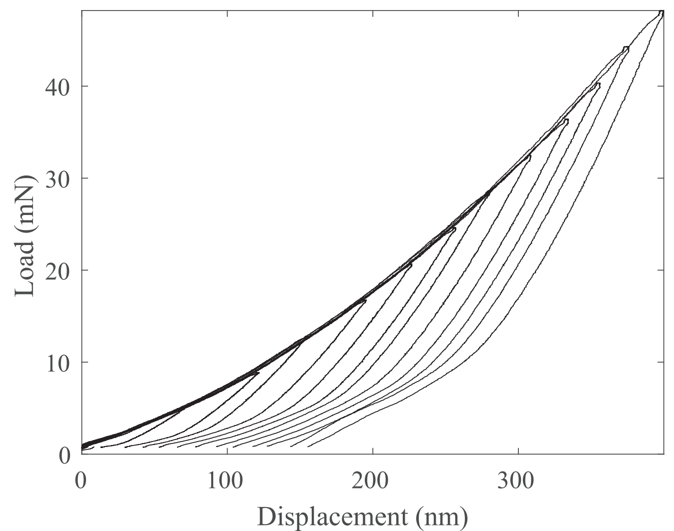

Fig. 3. Silicon wafer load displacement curves.

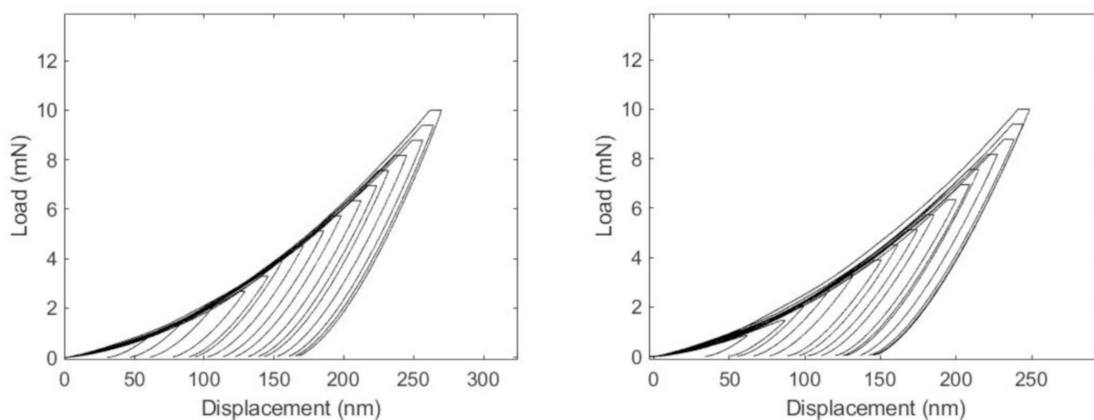

Fig. 4. Shallow load–displacement curves 1.5 μm (left) and 1.9 μm (right) film.

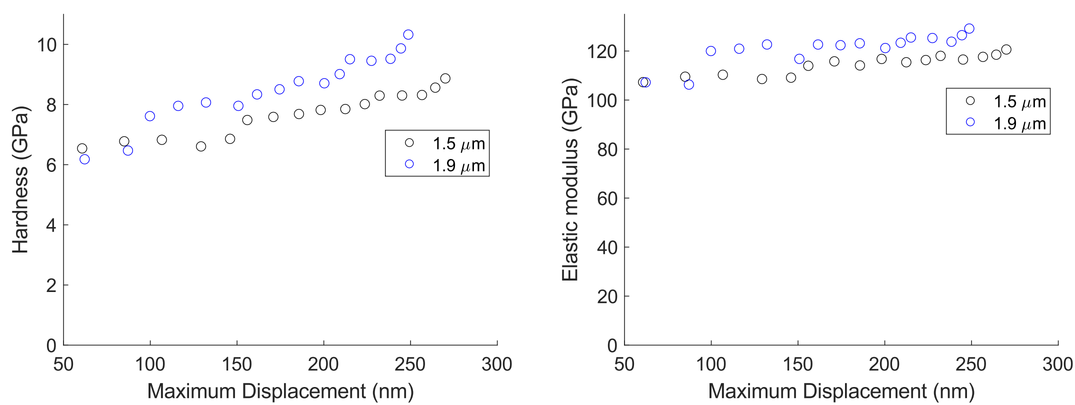

Fig. 5. Hardness (left) and Young's Modulus (right) as a function of maximum indentation depth.

Table 3
Mechanical properties of films from shallow indents.

	E (GPa)	H (GPa)
1.5 μm	108 ± 2	6.7 ± 0.3
1.9 μm	118 ± 6.1	7.8 ± 0.9

2. Materials and methods

2.1. Materials and Processing

Tungsten films were deposited onto silicon substrates using magnetron sputtering in a custom sputtering system equipped with two axially mounted AJA ST20-HV Radio Frequency (RF) sputtering guns. The substrates were mounted onto a central target block which gave a target-substrate distance of 18 cm. The films were deposited onto (001) orientated Si substrates that were first rinsed with acetone, isopropanol, and deionised water and dried with compress nitrogen. A 51 mm diameter W target with a purity of 99.95 % was used with an RF power of 100 W. The substrates were loaded into the sputtering chamber which was evacuated until a base pressure of $1x10^{-4}$ Pa was reached. Deposition was performed for a total of 6978 s (116.3 min) with an Ar working gas pressure of 2.5 Pa. The substrate was not rotated or externally heated during deposition.

Scanning Electron Microscopy (SEM) and Focused Ion Beam (FIB) Imaging were both performed using a Zeiss Auriga. FIB cross sectioning was used to cross-section the indent to verify delamination and to measure the film thickness with a tilt correction. Two thin films were selected for testing with thickness of 1.5 μm and 1.9 μm (referred to as the 1.5 μm and 1.9 μm films respectively). SEM imaging was conducted at 5 kV, while FIB milling used an accelerating voltage of 30 kV and a current of 4nA. The surface roughness of the two tungsten films was measured using in-situ Scanning Probe Microscopy (SPM), yielding an average roughness of 7 nm and 6 nm for the 1.5 μm and 1.9 μm film respectively.

2.2. Methods

2.2.1. Nanoindentation

Nanoindentation based delamination was performed at room temperature using a Bruker Premier Nanoindenter fitted with a high load head and a Berkovich tip. Calibrations were performed on fused silica to get an accurate tip area function for modulus and hardness measurements. A 50 μm spacing between indents was used to ensure no elastic zone overlap between indents. Indentation tests were conducted under load control in two regimes: a low-load regime (50–400 mN) and a high-load regime (100–1,000 mN) with 16 indents performed in each. The load profile used was a 5 s loading, 2 s hold, followed by a 5 s unloading. To investigate the effect of loading rate on delamination energy values, three different loading rates were tested: 52 mN/s, 104 mN/s and 260 mN/s. The delamination radius was obtained from SEM images of the indents by assuming the indent forms a perfect circle.

The elastic modulus and hardness values of the film were obtained through the Oliver Pharr method from shallow indents[24,25]. The shallow indents were done with a low load head with loads ranging from 1 to 10 mN, and 16 indents were performed in each sample.

2.2.2. Nanoscratching

Nanoscratching was performed using the same Premier nanoindenter and Berkovich tip using a high load transducer. Constant load scratch

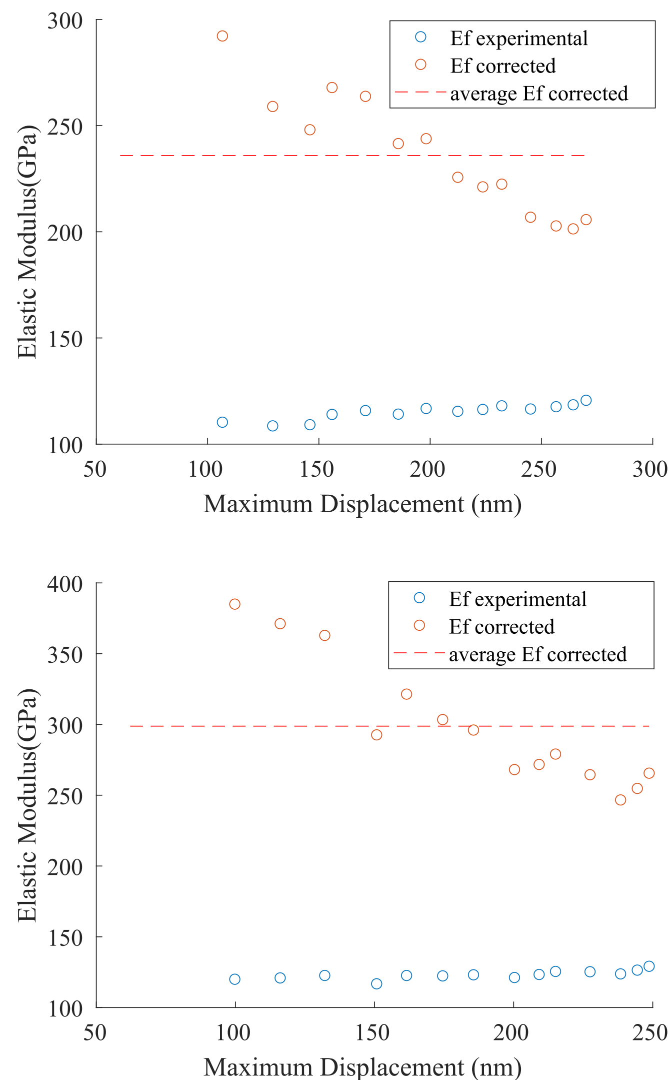

Fig. 6. Corrected elastic modulus for 1.5 film (top) and 1.9 film (bottom).

tests at 0.1 mN were performed to obtain the coefficient of friction ($\mu = F_{lateral}/F_{normal}$) needed for adhesion calculations[33]. Ramped load scratches with tilt correction were used to obtain the failure critical load with the following scratch parameters: peak load = 70 mN, scratch length = 250 μm, scratch time = 30 s. The main 3 scratch parameters that were varied in the parametric study were: scratch length, scratch maximum load, and scratch time. Additionally, scratches were performed in the edge forward and face forward direction to study the influence of scratch tip orientation (Fig. 1).

2.2.3. *Finite element modelling*

ABAQUS was used to conduct a finite element model (FEM) of the thin film indentation process. 1/6th of the sample and an ideally sharp Berkovich tip were modelled using axes of symmetry to simplify the computational time[34]. A description of the axes of symmetry and the geometry used in the model are shown in Fig. 2. The mesh elements used throughout the model were linear C3D8R elements. An optimal mesh with 10 elements across the cross-section of the thin film (0.19 μm mesh size) was found. A mesh bias was applied in the film and substrate regions to create a finer mesh near the indenter.

A thin film with a thickness of 1.9 μm was modelled on a 1 mm thick silicon substrate. The mechanical properties used for both materials are described in Table 2. The mechanical properties of the diamond indenter are not required as the tip was modelled as a rigid body. The system was modelled with an elastic-perfectly plastic thin film on a perfectly elastic substrate. Tungsten undergoes little to no strain hardening at room temperature due to its BCC structure, therefore this was not implemented in the model[35–37]. The modulus of the silicon wafer was obtained from nanoindentation experiments presented in the following section (E = 194 GPa), while the Poisson ratio was obtained from literature[34]. The nanoindentation results for the tungsten film in the subsequent section yielded underestimated modulus values. As a result, the modulus and yield strength of tungsten used in the FE models were taken from literature values instead[38–40].

The interaction between the indenter and the thin film was modelled as hard and frictionless with finite sliding. The boundary conditions used are: fixing the bottom of the substrate in the indentation direction (z-direction); fixing the sample and indenter planes of symmetry in the direction perpendicular to indentation (θ-direction using cylindrical coordinates); and the indenter was only allowed to move in the indentation direction (z-direction), which was displacement controlled to conduct the indentation test.

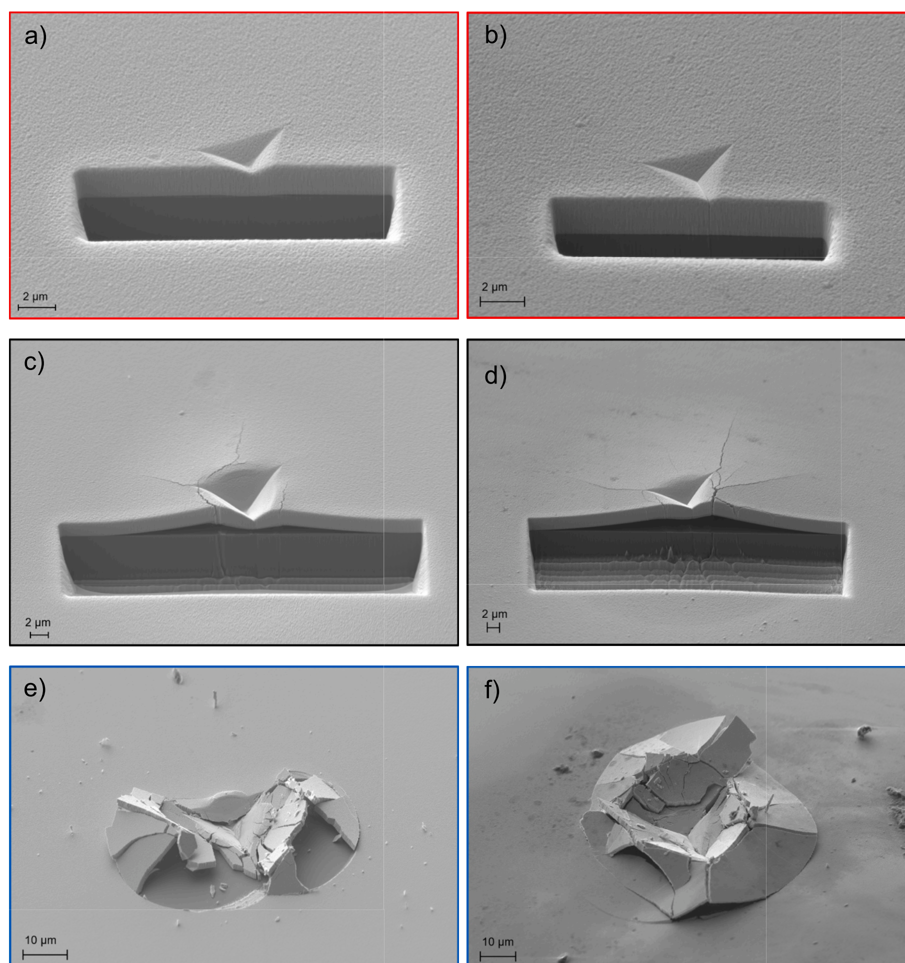

Fig. 7. SEM images of three stages of fracture observed in the 1.5 µm film (left) and 1.9 µm film (right) with applied loads of 73 mN (a, b), 370 mN (c, d), 760 mN (e, f).

Table 4
Summary of load ranges and maximum displacement ranges for 3 stages of deformation.

	1.5 µm	1.9 µm	Colour Code
Stage I – plastic deformation and surface cracks	< 73 mN < 700 nm	< 73 mN < 700 nm	Red
Stage II – blistering	97 mN – 377 mN 750 – 1500 nm	97 – 400 mN 780 – 1600 nm	Black
Stage III – fragmentation	> 400 mN > 1500 nm	> 460 mN > 1780 nm	Blue

3. Results and Discussion

3.1. Nanoindentation

3.1.1. Mechanical properties

Indentation tests were initially performed on an uncoated silicon substrate to characterize its properties. Fig. 3 shows the load displacement curves, from which an average of Young's modulus of 194.16 ± 1.31 GPa and an average hardness of 13.99 ± 1.56 GPa was found.

Load-displacement curves on the thin films performed in the shallow depth regime are shown in Fig. 4. The reduced modulus obtained from the nanoindenter was converted to the true elastic modulus using the properties of the diamond indenter (E = 1140 GPa, ν = 0.07) provided by the manufacturer. The Young's modulus (E) and hardness (H) are plotted as a function of maximum indentation depth in Fig. 5. The values of Young's modulus and hardness increase with increasing indentation depths due to a greater interaction with the substrate[41]. The values of hardness and Young's modulus shown in Table 3 are an average of the indents with a maximum depth less than 10 % of the total film thickness to evaluate the applicability of this criterion in minimizing substrate influence[38,41].

The hardness values obtained from shallow indents are close to that of bulk tungsten (6 GPa)[42], however the Young's modulus is significantly lower than bulk tungsten (410 GPa)[43]. Similar results showing correct hardness and incorrect elastic modulus film values were found in literature[34,44]. FEM analysis of thin films showed that while it is possible to contain the plastic regime within the film to determine hardness, containing the elastic regime is difficult even at shallow depths[34].

To correct for the substrate effects, the modified King expression developed by Saha and Nix[45] was used and the corrected average Young's modulus of the films were found to be 236 ± 27 GPa and 300 ± 45 GPa, for the 1.5 µm and 1.9 µm film respectively (Fig. 6). Surface effects observed up to a maximum displacement of 100 nm introduced deviations in the average values. Therefore, the first two data points were excluded from the calculations. The 1.9 µm sample exhibited higher uncorrected and corrected modulus values compared to the 1.5 µm film. This can be attributed to reduced substrate effects in the thicker film at any given depth. However, the corrected modulus for the 1.9 µm film remained lower than that of bulk tungsten. Similar underestimated

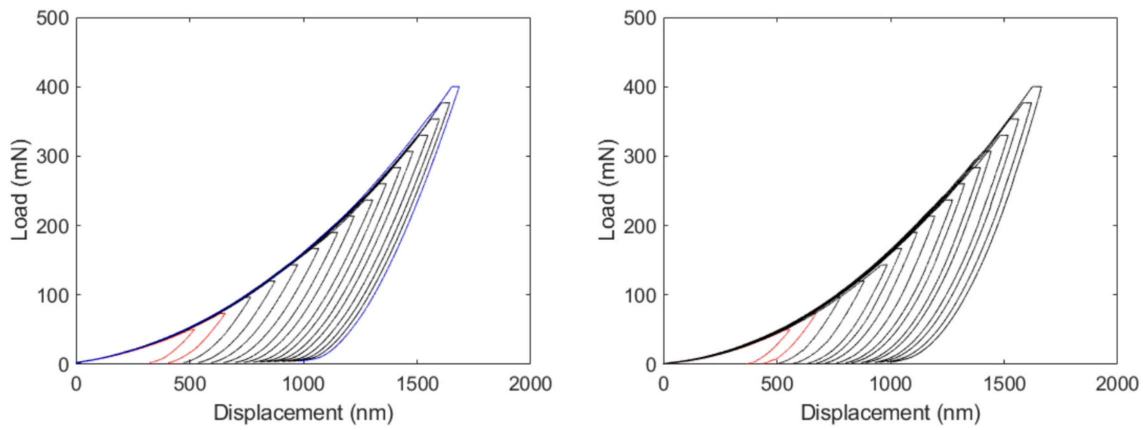

Fig. 8. Low load displacement curves 1.5 µm (left) and 1.9 µm (right). Red: plastic deformation, black: blistering, and blue: fragmentation.

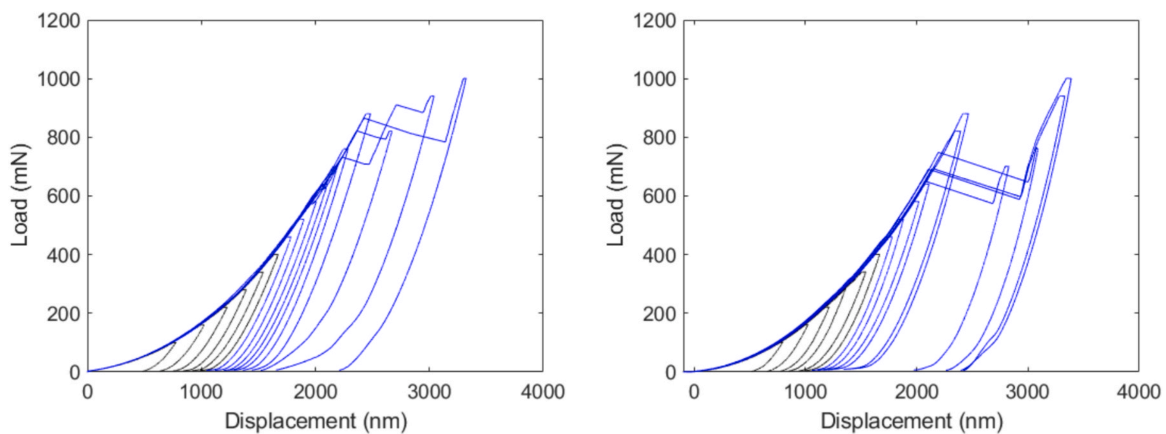

Fig. 9. High load displacement curves 1.5 µm (left) and 1.9 µm (right). Black: blistering, and blue: fragmentation.

values for tungsten after applying substrate corrections have been reported in the literature (E = 370 GPa)[39], potentially due to porosity or other fabrication defects.

3.1.2. Nanoindentation adhesion

Indentation was conducted on both samples in a low load range (50–400 mN) and a high load (100–1,000 mN). SEM images at three different peak loads of 73 mN, 370 mN, and 760 mN are shown in Fig. 7, showing stages of plastic deformation (a,b), blistering and delamination (c,d), and fragmentation (e,f) respectively. The load ranges and maximum indentation depths observed in each stage is summarized in Table 4.

The low load and high load displacement curves are given in Figs. 8 and 9 respectively. Both samples display no observable slope change in the load displacement curves for the low load tests, and significant steps in the high load curves. SEM and FIB images in Fig. 7 highlight three distinct stages of deformation during loading. Firstly, minimal plastic deformation and radial cracks were observed in the lowest load regime (stage I). As the loads increased, circular blisters began forming on the surface (stage II). These blisters are indicative of film delamination which are observed subsurface using FIB, Fig. 7 (c, d). This is formed because double buckling occurs around the indenter as the indenter is driven into the film[46]. Then as the indenter is removed, the portion of the film under the indenter is no longer pinned and forms a circular raised blister. The radius of the blister was observed to increase as the maximum load increased. This indicates that delamination in this sample is gradual and not an instantaneous event, which explains the lack of slope deviation in the load–displacement curves and agrees with other observations in the literature[32]. During stage II, additional cracks appear and the radial cracks grew to a critical length while increasing in width. No major substrate cracking was observed in this stage, which ensures that the delamination energy is not overestimated. The features visible in the SEM images in the substrate under the indent are an effect of FIB curtaining and not substrate cracking.

The final stage occurs as the blister reaches a critical radius, after which fragmentation occurs as seen in Fig. 7 (e, f). Some curves in the fragmentation regime (blue curves in Fig. 9) avoid fragmentation above the critical fragmentation load. This can be attributed to statistical effects and localized adhesive strength inhomogeneity due to the sputtering fabrication process. FIB and SEM imaging shows that delamination occurs before the occurrence of the large load–displacement steps (observed at large depths in Fig. 9). From this observation we conclude that these steps in the loading curve are due to film fragmentation alone.

The load–displacement curves can be analysed through the energy approach described by Malzbender[22] to determine the work of delamination, prior to the large depth discontinuities. This method was selected as it is applicable to data where there is no significant step in the load–displacement curve on delamination. The area enclosed by the load–displacement curve gives us the irreversible work done by the indenter, including plastic deformation, delamination, and fragmentation. The total irreversible work for each stage of fracture is described in Eqs. (3)–(5) below.

$$StageI : W_{irr} = W_p \tag{3}$$

$$StageII : W_{irr} = W_p + W_d \tag{4}$$

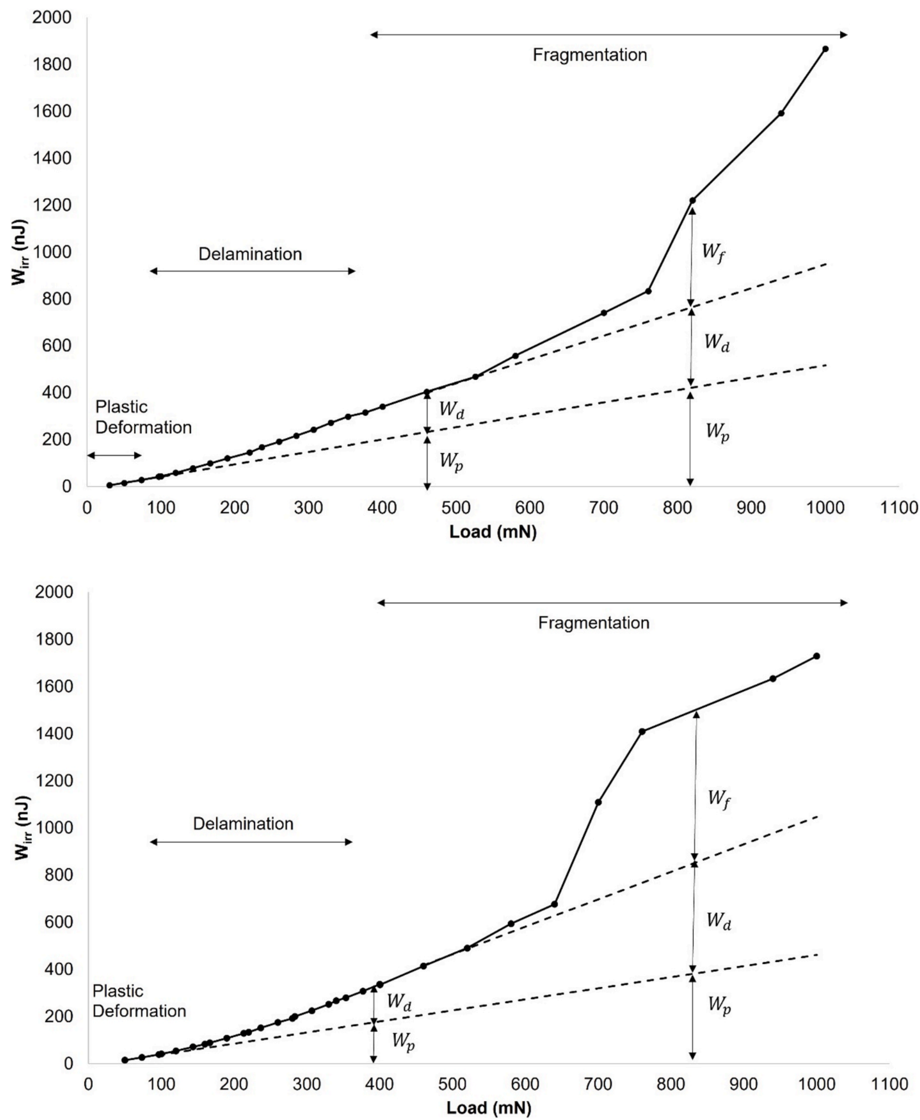

Fig. 10. Irreversible work done (W_{irr}) vs load map for 1.5 μm film (top) and 1.9 μm film (bottom). Work of delamination (W_d) calculated as the difference between W_{irr} and plastic work (W_p).

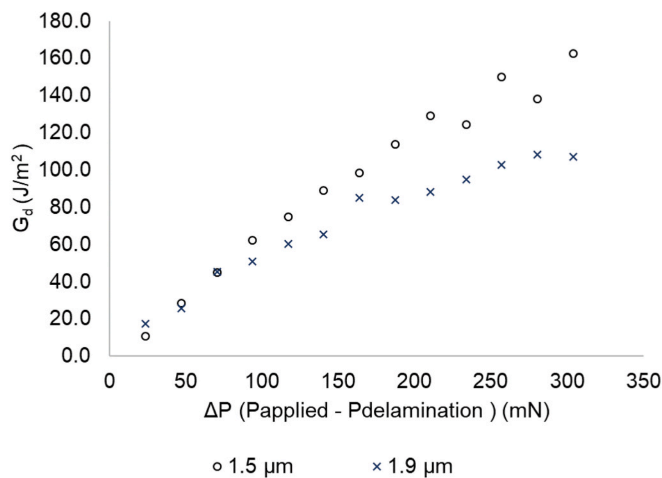

Fig. 11. Plot of delamination energy G against ΔP= $P_{applied}$-$P_{delamination}$.

Table 5
Summary of range of delamination energies calculated.

	1.5 μm	1.9 μm
Range of delamination energies	11–162 J/m^2	17–107 J/m^2

$$StageIII : W_{irr} = W_p + W_d + W_f \tag{5}$$

Where W_p is the plastic work, W_d is the work of delamination, and W_f is the work of fragmentation. The other energy-based analysis methods [19,20] use a power law to extrapolate the loading curve, which is applicable for bulk materials however it is unclear whether a power law is applicable to thin films due to the effect of the substrate.

The irreversible work is plotted against the applied load in the Fig. 10. Malzbender suggests that the plastic work W_p can be linearly extrapolated from the experimental data in stage I. The work of delamination in stage II is calculated as the difference between the experimental line and the extrapolated plastic work line. The line of delamination work is also linearly extrapolated from stage II to allow for fragmentation energy calculations in stage III. This assumes that other dissipation mechanisms (i.e. plastic deformation due to buckling and

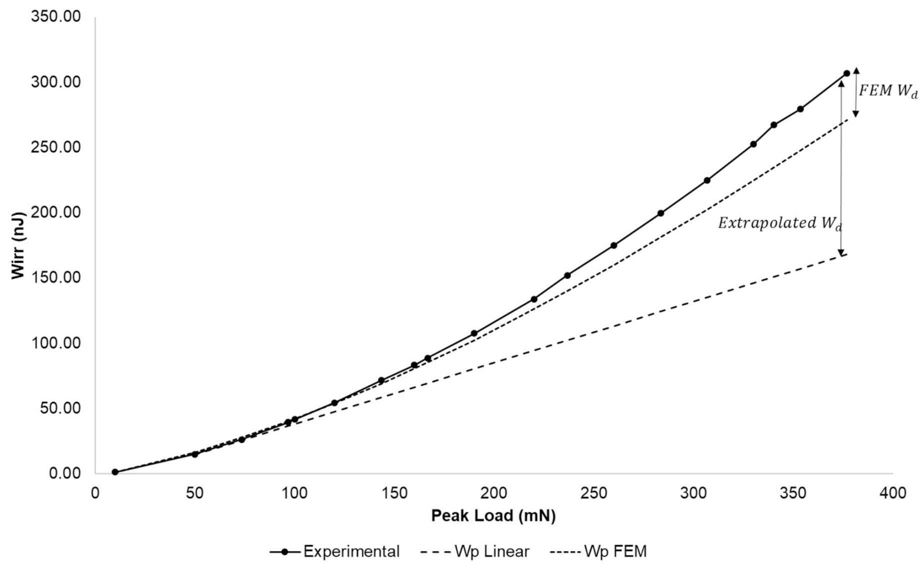

Fig. 12. Irreversible work map in the stage I and II regime with the linearly extrapolated, FEM and experimental curves. FEM W_d is calculated as (W_{irr}-$W_{p(FEM)}$), while extrapolated W_d is calculated as (W_{irr}-$W_{p(extraploated)}$)).

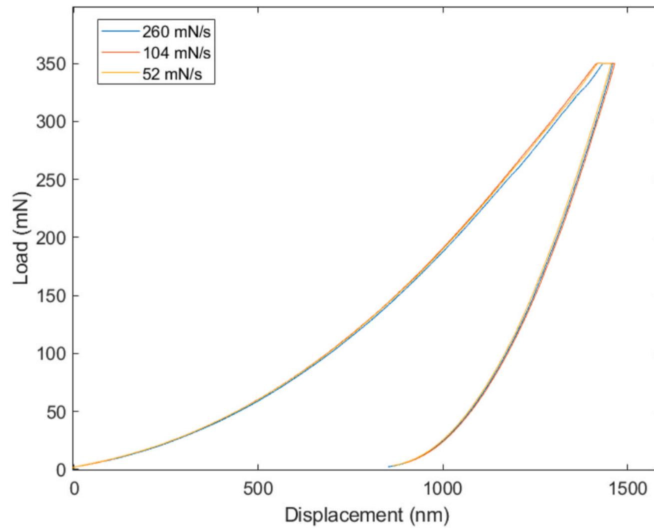

Fig. 13. Load displacement curve for three different loading rates.

substrate deformation) have a minimal contribution to the irreversible work.

Finally, the delamination energy can then be calculated as follows:

$$G_d = \frac{W_d}{\pi r^2} \tag{6}$$

Where r is the blister radius.

Considering indents in stage II allows for accurate determination of delamination energy without any fragmentation effects. The SEM images indicate that fragmentation is an event arising from fracture in the thin film itself and not the interface.

The values calculated for the delamination energy are plotted in Fig. 11 against the difference between the applied load and the initial delamination load, summarized in Table 5. The delamination energy increases with the applied load for both samples. This agrees with the gradual increase in delamination observed by SEM with increasing load. It is possible that the delamination energy is being overestimated at high loads as the indenter gets closer to the interface as there may be an increasing influence of the substrate.

Similar delamination energies were measured for the two films at low loads while at higher loads, lower values of delamination energy were measured for the 1.9 μm than the 1.5 μm. This behaviour is due to a combination of two different reasons. There is a greater contribution from the substrate in the thinner samples at the same load (or absolute depth) compared to the thicker samples, which leads to an increase in the measured delamination energy[22]. The second reason is that there may be a difference in the residual stresses of the two samples. An increase in thickness leads to higher amounts of stored elastic energy in the film, which are released to induce delamination and fracture[24].

3.1.3. FEM corrected method

The assumption of linear extrapolated work in the method described in the previous section was investigated using an FEM simulation of the 1.9 μm film. The model only considers the total irreversible work due to plastic dissipation without delamination or fragmentation. The simulation appropriately models the plastic dissipation work in the thin film as shown by the agreement of the FEM and experimental W_{irr} value in the low load regime (<97 mN) before any delamination occurs. Fig. 12

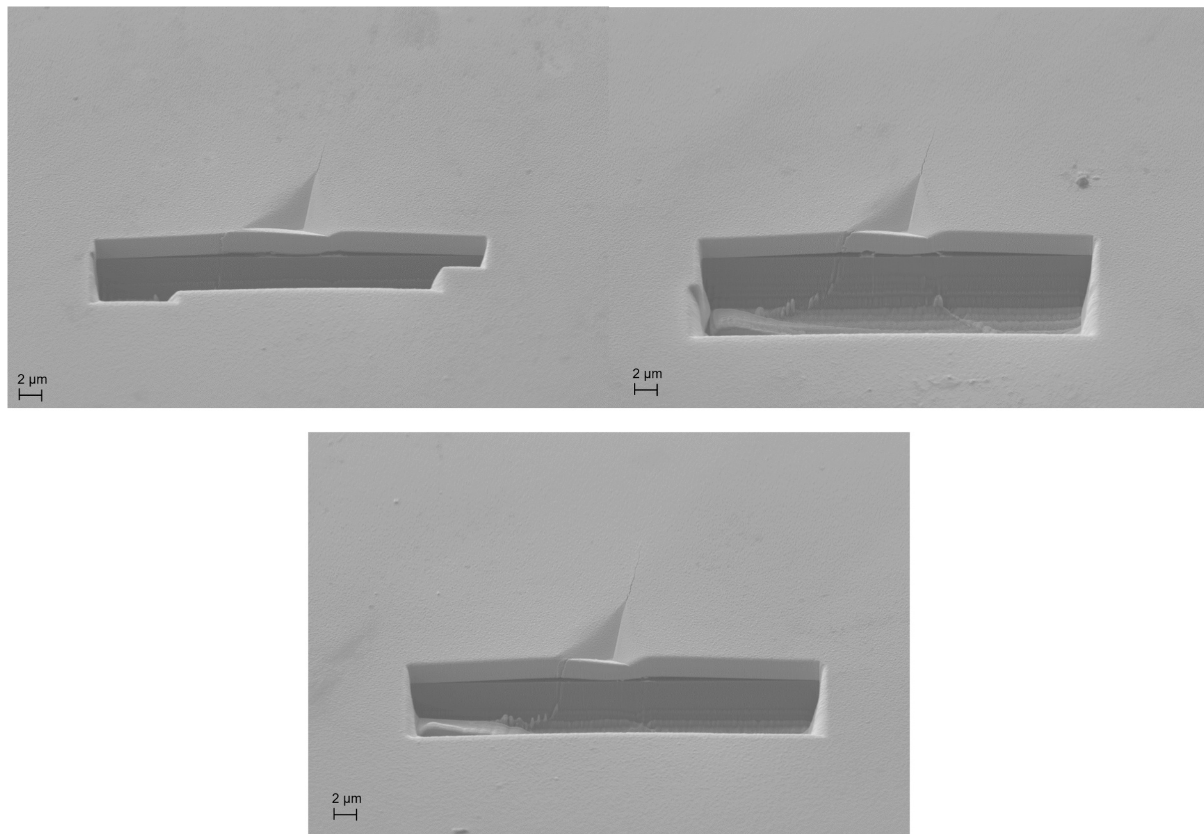

Fig. 14. SEM images of indents with three different loading rates of 260 mN/s (top left), 104 mN/s (top right), 52 mN/s (bottom).

Table 6
Values of delamination energy with different loading rates.

	Blister Radius (μm)	W_{irr}(nJ)	W_d(nJ)	G (J/m^2)
260 mN/s	17	268.7	21.7	23.9
104 mN/s	17.3	274.7	27.7	29.5
52 mN/s	17.8	269.8	22.8	23.0

shows the values of the FEM calculated values of irreversible work for a range of peak loads compared with the experimental values, and the linear extrapolation from the plastic deformation in stage I (as performed in the previous section).

The FEM data suggests that the plastic dissipation work does not follow the linear progression proposed by Malzbender[22] and that using a linear extrapolation significantly overestimates the value of the work of delamination. Others reporting this overestimation suggest that this is due to additional energy dissipation mechanisms that cannot be separated from delamination[32,47].

Our FEM simulation allows for these mechanisms to be captured and results in a smaller range of measured delamination energies (2–29 J/m^2) with increasing peak loads compared with those calculated with the linear extrapolation (17–107 J/m^2). This is due to the smaller work of delamination calculated from the FEM plastic work compared to the linear extrapolated plastic work. This reduction in uncertainty in the measured delamination energy provides values that agree well with the adhesion of tungsten on silicon measured by other methods[18,39,48].

3.1.4. The influence of loading rate

Three sets of indents were performed on the 1.9 μm film using the following loading rates 52, 104 and 206 mN/s with an applied load of 350 mN. No change was observed in the load–displacement curves for the different loading rates, as seen in Fig. 13. The SEM images show that the 3 indents reached a similar level of delamination (Fig. 14). Table 6 summarizes the similarity in calculated delamination energy from all three indents due to the same load–displacement curve shape and similar delamination radii. This suggests that the loading rate has no effect on delamination energy values and that the delamination mechanism is strain rate independent.

3.2. Nanoscratch

3.2.1. Nanoscratch adhesion

Ramped load scratches with maximum load of 70 mN were performed on both samples and observed by SEM (Fig. 15). Both scratches display plastic deformation initially, followed by sudden fragmentation (or spallation) at the critical point of failure[30]. The thin film material behind the indenter was removed at the point of critical failure as the tensile stress is concentrated on the rear of the indenter while scratching [49]. Fragmentation is expected to be the dominant failure mode for a hard coating on a hard substrate[50]. No buckling or blistering is observed in the initial portions of the scratch.

The normal force and friction coefficient during the ramped portion are plotted in Fig. 16. Failure in a scratch test is denoted by a sudden change in the graph of friction coefficient and normal force. The 1.5 μm

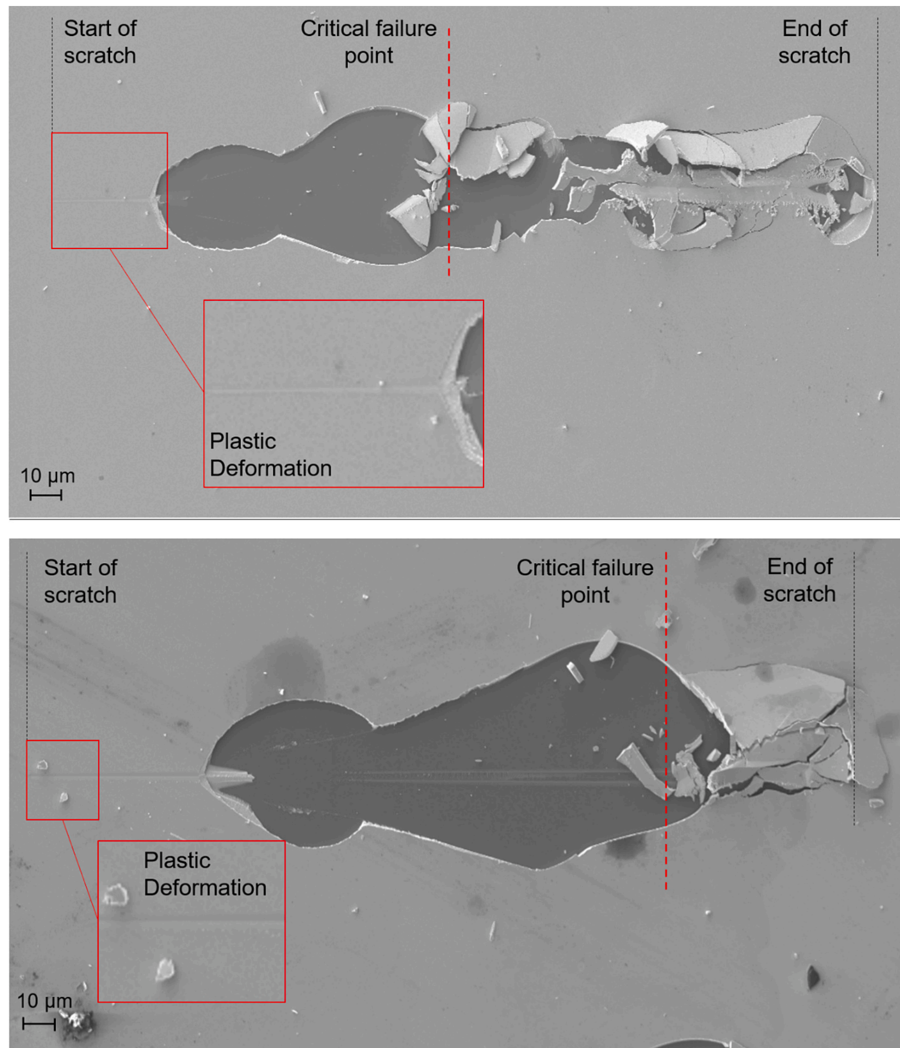

Fig. 15. SEM images of example scratches on 1.5 µm film (top) and 1.9 µm film (bottom) made with a maximum load of 70 mN, scratch time of 30 s, and scratch length of 250 µm.

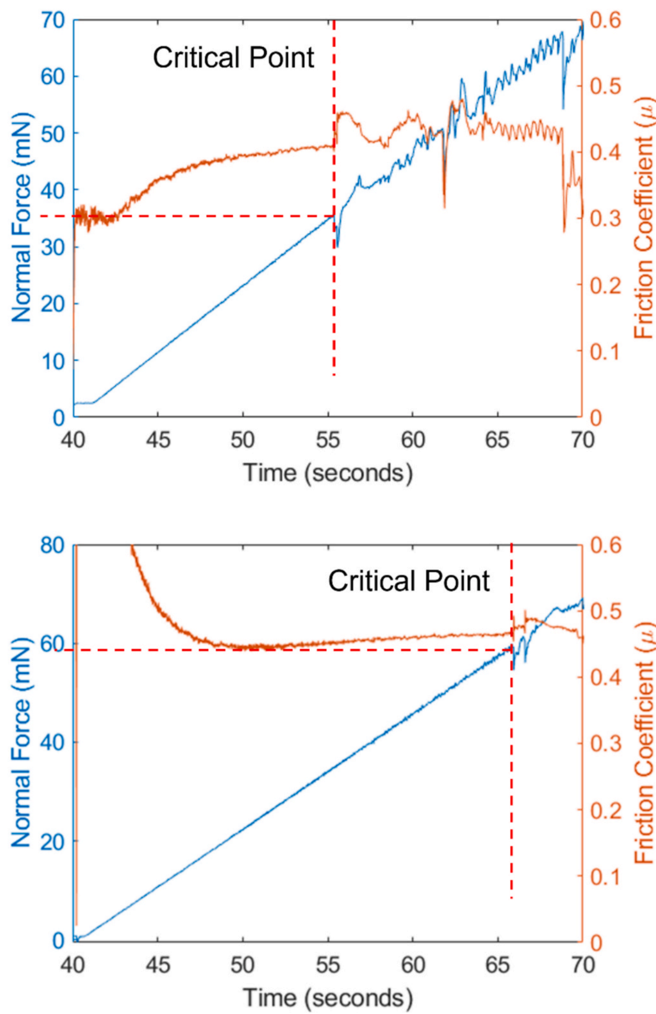

Fig. 16. Normal force and friction coefficient graphs for 1.5 μm (top) and 1.9 μm (bottom), red dotted line indicates the critical point of failure (P_c).

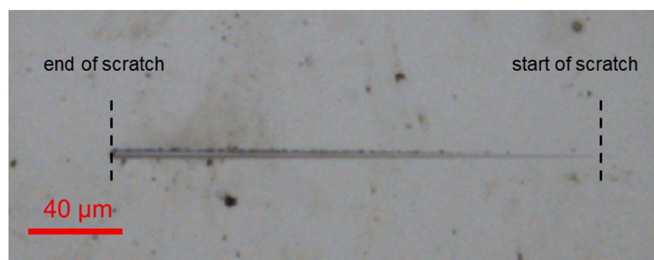

Fig. 17. Scratch at 30 mN peak load on 1.9 μm film.

Table 7
Properties at point of critical scratch failure.

	P_c(mN)	d_c(μm)	ν_f	μ	E_f(GPa)	σ(GPa)	$G_d(J/m^2)$
1.5 μm	35	2.22	0.28	0.3	410	4.8	43
1.9 μm	58	3.42	0.28	0.3	410	3.4	27

film displayed a lower critical load of 35 mN, while the 1.9 μm film fails at around 58 mN. This is expected as a thicker film will need a higher load to fail compared to a thinner film[51–53]. More load is dissipated in the thicker film before being transferred to the interface, leading to a higher critical load needed to delaminate the interface.

The Laugier model[26] gives the adhesive strength of the interface (σ) as:

$$\sigma = \left(\frac{2P_c}{\pi d_c^2}\right)\left[\frac{(4+\nu_f)3\pi\mu}{8} - (1-2\nu_f)\right] \tag{7}$$

Where P_c is the critical load, d_c is the critical scratch width, ν_f is the film Poisson ratio, and μ is the film coefficient of friction. The scratch width at the point of failure in Eq. (7) cannot be measured directly from the residual SEM image due to fragmentation, therefore it is calculated from the tip geometry and contact depth, assuming a perfectly sharp tip.

$$d_c = \frac{2h_c}{tan\alpha} \tag{8}$$

Where h_c is the contact depth and α: is the effective cone angle.

To study the validity of the Eq. (8), a scratch with peak load 30 mN was performed on the 1.9 μm film (Fig. 17). This peak load was less than the critical load, so no fragmentation took place and the scratch width at peak load was measured through optical microscopy to be 2.24 μm. Using the contact depth, the equation above outputted a scratch width of 2.71 μm, meaning that Eq. (8) can accurately determine scratch width from contact depth.

Adhesive strength is related to the adhesive energy by:

$$G_d = \frac{\sigma^2 t}{2E_f} \tag{9}$$

Where t is the film thickness and E_f is the modulus of the film.

The values of these parameters for both films are given in Table 7, along with the calculated adhesive strength and delamination energy. Since the elastic modulus of the tungsten film was underestimated in the previous nanoindentation results, the modulus used for the calculations was instead based on bulk tungsten values[43]. The friction coefficient used in the Laugier calculations ($\mu = 0.3$) was found from low load scratches (<10 mN) ensuring minimal contribution from material removal or ploughing friction.

The thicker (1.9 μm) film produced a lower value of delamination energy due to the higher scratch width despite the higher critical load compared with the thinner film. The film thickness is an intrinsic parameter that affects the results of the scratch tests, so direct comparisons between the delamination energies of the two samples cannot be made here. The large film fragments observed in the post-scratch SEM images suggests that the real adhesive strength of the film is low, therefore the calculated delamination energies may be overestimated. Additionally, the occurrence of severe fragmentation also means that the calculated adhesion energy measured will contain a contribution from the film fracture energy.

3.2.2. *Influence of scratch parameters*

Comparison of scratch results in the literature is difficult due to the high sensitivity to scratch parameters. This section is included to show the wide range of delamination energy values that are measured from the scratch test by changing the testing parameters. Table 8 shows all the combinations of parameters that were tested on the 1.9 μm film (face forward orientation) with the resultant measured critical load and delamination energy calculated.

The critical load varies measurably with all these parameters and shows a significant positive correlation with the ratio of dL/dx, which agrees with previous observations[27,51]. An increase in dL/dx decreases the probability of encountering an interfacial defect, leading to higher value of critical load. No direct dependence on either dL/dt or dx/dt alone was found on the critical load.

Failure was seen to occur in a large range of contact depths values ranging from 610 nm to 1,900 nm. No failure was observed at contact depths greater than 1,900 nm (equal to the film thickness). A range of delamination energies were calculated ranging from $12 - 27\ J/m^2$.

Table 8
Various combinations of scratch parameters tested on 1.9 µm film along with critical load and delamination energy.

Peak Load (mN)	Scratch Length (um)	Scratch Time (s)	dL/dt	dx/dt	dL/dx	P_c (mN)	hc (nm)	G (J/m^2)
70	250	30	2.33	8.33	0.28	58	610	27
100	180	30	3.33	6.00	0.56	73	717	22
200	250	30	6.67	8.33	0.80	79	751	22
100	100	60	1.67	1.67	1.00	76	720	24
250	200	30	8.33	6.67	1.25	90	810	21
250	100	30	8.33	3.33	2.50	125	980	19
400	100	30	13.33	3.33	4.00	177	1244	15
300	60	10	30.00	6.00	5.00	173	1182	17
500	50	10	50.00	5.00	10.00	118	1003	15
300	20	30	10.00	0.67	15.00	159	1213	13
400	20	30	13.33	0.67	20.00	202	1400	12
600	20	30	20.00	0.67	30.00	237	1494	13
800	20	30	26.67	0.67	40.00	383	1907	12
500	10	5	100.00	2.00	50.00	no failure	–	–

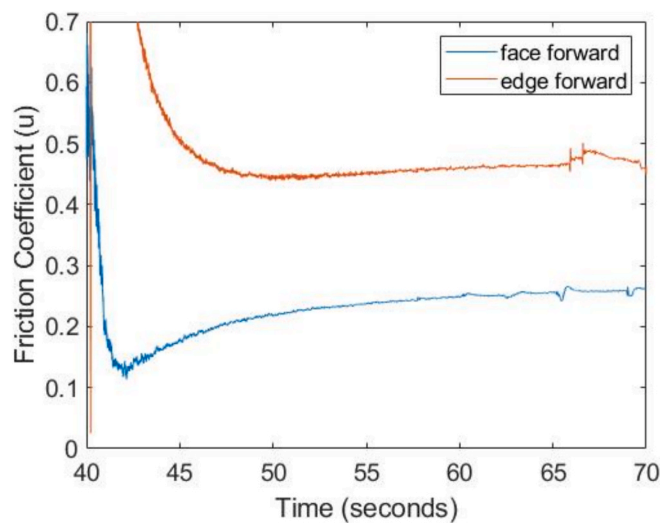

Fig. 18. Friction coefficient graphs for the face and edge forward orientation.

Generally, lower values of adhesive energy were obtained with higher ratios of dL/dx and no failure was observed with dL/dx ratios above 40.

Scratches were performed in both the edge forward face and the face forward face to investigate the influence of the scratch orientation on delamination energy, for a set of different scratch parameters. Fig. 18 shows the friction coefficient graph for the edge forward and face forward orientation using the same scratch parameters of 70 mN load, 250 µm scratch length and 30 s scratch time. The edge forward direction produced higher friction coefficient values compared to the face forward case, agreeing with the results of Wang et al[54]. The critical loads recorded along with the delamination energy of each is summarized in Table 9. Edge forward orientation was found to produce higher values of both critical load and delamination energy, with a range of delamination energies of 25–49 J/m^2 (depending on the parameters selected) as compared to 13–27 J/m^2 from the face forward orientation. Wang et al. [54] have shown that the face forward orientation is more likely to initiate lateral crack formation in the sample, which explains the lower critical loads found in our experiments.

3.3. Comparison and discussion of feasibility of both methods

Nanoscratch and nanoindentation experiments have been shown to display different deformation mechanics. In nanoindentation, the indent progresses from plastic deformation and surface cracking, to blistering, and finally fragmentation. In the nanoscratch experiments, the scratch progressed from plastic deformation to sudden fragmentation. The critical loads needed to induce fragmentation in the nanoindentation tests (400 mN and 460 mN for the 1.5 µm and 1.9 µm film, respectively) were much higher than the critical loads for fragmentation seen in the nanoscratch tests (35 mN and 58 mN for 1.5 µm and 1.9 µm film, respectively). It is expected that the load needed to induce fragmentation should be higher in nanoindentation since only one force is involved

Table 10
Comparison of range of delamination energies calculated from nanoindentation and nanoscratch test for the 1.9 µm film, along with literature values of tungsten on silicon thin films.

	Delamination Energy
Nanoindentation (using FEM correction)	2–29 J/m^2
Nanoscratch	13–49 J/m^2
Literature values of tungsten on silicon[18,39,48]	5–15 J/m^2

Table 9
Effect of scratch tip orientation on critical load and delamination energy.

Peak Load (mN)	Scratch Length (µm)	Scratch Time (s)	dL/dt	dx/dt	dL/dx	P_c (mN)	hc (nm)	G (J/m^2)
Face Forward								
70	250	30	2.33	8.33	0.28	58	610	27
400	100	30	13.33	3.33	4.00	177	1244	15
300	60	10	30.00	6.00	5.00	173	1182	17
600	20	30	20.00	0.67	30.00	237	1494	13
Edge Forward								
70	250	30	2.33	8.33	0.28	40	437	49
400	100	30	13.33	3.33	4.00	197	1099	30
300	60	10	30.00	6.00	5.00	209	1160	27
600	20	30	20.00	0.67	30.00	443	1722	25

(normal force), meanwhile the presence of two loads (normal and lateral) in nanoscratch, lowers the normal load needed for fragmentation.

Table 10 summarized the values of delamination energies calculated from the nanoindentation method using FEM data and from the nanoscratch test. Nanoscratch is seen to give higher values of delamination energy as compared to nanoindentation because the energy of film fragmentation is included in the delamination energy calculations. The scratch analysis developed by Laugier[26] assumes that the work done by the indenter to fragment the film is small compared to the delamination work, which is not the case for our experiments. Fragmentation significantly increases the total work during nanoindentation (Fig. 10) suggesting that fragmentation will also have a significant contribution to the total work done during scratch. The nanoindentation test with FEM corrections was found to output results agreeing with literature[39,48]. Comparable values of G were found using the nanoscratch test with high dL/dx ratios, with the face forward orientation.

The high parameter sensitivity combined with a lack of a standardized parameter selection process for nanoscratching makes the semi-quantitative values of delamination energy results difficult to interpret. The nanoindentation test is not parameter sensitive and is able to provide quantitative values of adhesion which agree very well with values obtained by other methods in the literature[18,39,48].

4. Conclusions

Through nanoindentation, film hardness properties comparable to bulk tungsten were found due to the plastic zone being contained within the film at these depths. On the other hand, the Young's modulus had high substrate effects, leading to underestimated values (118 GPa). Corrections to the Young's modulus led to values (300 GPa) closer to that of bulk tungsten.

Interface delamination energy was measured using two different methods; nanoindentation and nanoscratching. In nanoindentation adhesion analysis, conventional linear extrapolation of the plastic dissipated work resulted in a range of delamination energy values of 11–162 J/m^2 and 17–107 J/m^2 from the 1.5 μm and 1.9 μm film, respectively. FEM simulations of the 1.9 μm film allowed for the plastic dissipated work to be corrected to give a range of delamination energies of 2–29 J/m^2, agreeing more closely with literature.

Different deformation mechanics were observed in nanoscratch tests. The scratch progressed from plastic deformation directly to fragmentation. Tests with a similar set of scratch parameters produced values of adhesive energy for 1.5 μm and 1.9 μm film were found to be 43 J/m^2 and 27 J/m^2 respectively. Different scratch parameter combinations were used to show their effect on the values of delamination energy ranging from 13 to 49 J/m^2. Higher values of dL/dx were found to give higher critical loads and lower delamination energies. The scratch orientation was found to be an important parameter that significantly altered the delamination energy, with face forward orientation outputting lower delamination energy values as compared to edge forward. Nanoscratch adhesion values comparable to those outputted from nanoindentation and literature were found using high dL/dx ratios and a face forward orientation. While the observed trends align with findings in the literature, additional scratches under the same conditions would further reinforce the statistical significance of these results.

This paper has highlighted the difference in adhesion energies measured by nanoindentation and nanoscratching. Nanoindentation measurements showed that fragmentation is an important event that causes an overestimation of the calculated adhesion energy. Further work needs to be done on scratch testing to understand the effect of adhesion energy overestimation caused by fragmentation.

CRediT authorship contribution statement

Shatha Almarri: Writing – original draft, Methodology, Investigation, Data curation. **Matthew Lloyd:** Resources. **Ed Darbrough:** Writing – review & editing, Supervision. **David Armstrong:** Writing – review & editing, Supervision.

Declaration of competing interest

The authors declare the following financial interests/personal relationships which may be considered as potential competing interests: Shatha Almarri reports financial support was provided by United Arab Emirates Ministry of Education. This research was also funded in part, by the UKRI Faraday Institution [SOLBAT FIRG026 and FIRG056]. For the purpose of Open Access, the author has applied a CC BY public copyright license to any Author Accepted Manuscript version arising from this submission. The authors acknowledge use of characterization facilities within the David Cockayne Centre for Electron Microscopy, Department of Materials, University of Oxford, alongside financial support provided by the Henry Royce Institute (Grant ref EP/R010145/1).

Acknowledgements

Shatha Almarri reports financial support was provided by United Arab Emirates Ministry of Education. This research was also funded in part, by the UKRI Faraday Institution [SOLBAT FIRG026 and FIRG056]. For the purpose of Open Access, the author has applied a CC BY public copyright license to any Author Accepted Manuscript version arising from this submission. The authors acknowledge use of characterization facilities within the David Cockayne Centre for Electron Microscopy, Department of Materials, University of Oxford, alongside financial support provided by the Henry Royce Institute (Grant ref EP/R010145/1).

Appendix

A mesh convergence study on the effect of mesh on load–displacement curve (indirectly measured through Wirr i.e: area under curve). The number of mesh elements in the film regions shown with a red arrow (under the indenter) was varied for convergence.

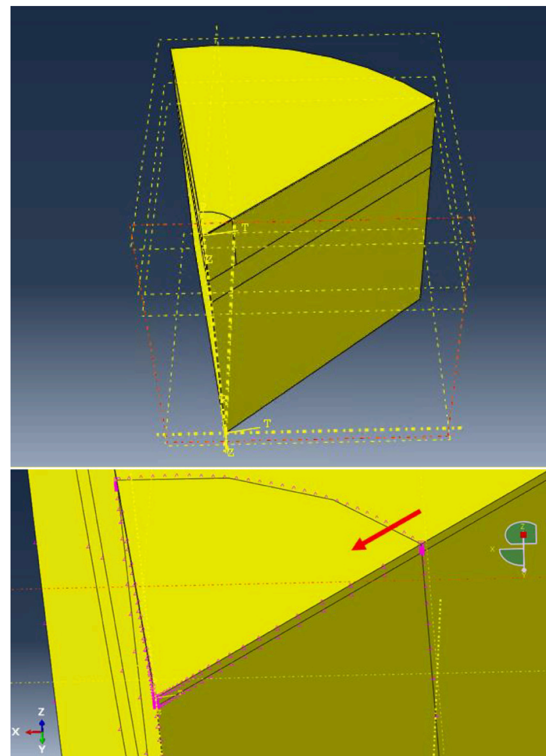

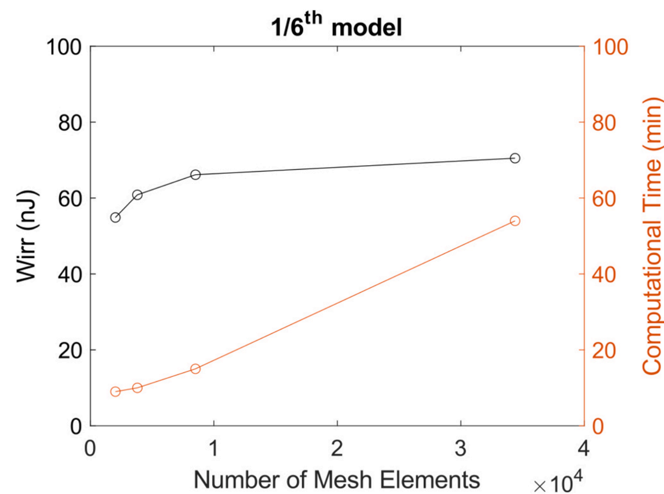

$1x10^4$ mesh elements was selected as optimal mesh size for modelling.

Data availability

Data will be made available on request.

References

[1] Q.T. Miao, years of N-heteropentacenes as semiconductors for organic thin-film transistors, Adv. Mater. 26 (2014) 5541–5549.

[2] M.A. Butt, Thin-Film Coating Methods: A Successful Marriage of High-Quality and Cost-Effectiveness—A Brief Exploration, Coatings 12 (2022).

[3] N.J. Dudney, B.J. Neudecker, Solid state thin-film lithium battery systems, Curr. Opin. Solid State Mater. Sci. 4 (1999) 479–482.

[4] M. Koo, et al., Bendable inorganic thin-film battery for fully flexible electronic systems, Nano Lett 12 (2012) 4810–4816.

[5] T.I.T. Okpalugo, A.A. Ogwu, DLC thin films for implantable medical devices, Thin Film Coati. Biomater. Biomed. App. 261–287 (2016), https://doi.org/10.1016/B978-1-78242-453-6.00011-0.

[6] M. Edoff, Thin film solar cells: Research in an industrial perspective, Ambio. 41 (2012) 112–118.

[7] M. Sathish, N. Radhika, B. Saleh, Current status, challenges, and future prospects of thin film coating techniques and coating structures, J. Bio-Tribocorrosion. 9 (2023). Springer International Publishing.

[8] N. Sharma, M. Hooda, S.K. Sharma, Stresses in thin films: an experimental study, Indian J. Phys. 93 (2019) 159–167.

[9] D.E. Packham, Work of adhesion: Contact angles and contact mechanics, Int J Adhes Adhes 16 (1996) 121–128.

[10] K.L. Mittal, Adhesion Measurement of Thin Films, Electrocompon. Sci. Technol. 3 (1976) 21–42.

[11] M. Rezaee, et al., Quantitative peel test for thin films/layers based on a coupled parametric and statistical study, Sci. Rep. 9 (2019) 1–11.

[12] Z. Liu, J. Sun, J.D. Wu, P.N. Wang, W. Shen, Determination of adhesion energy of cnx thin film on silicon from micro-scratch testing, Tribol. Trans. 47 (2004) 130–137.
[13] C. Julia-Schmutz, H.E. Hintermann, Microscratch testing to characterize the adhesion of thin layers, Surf. Coat. Technol. 48 (1991) 1–6.
[14] N. Panich, Y. Sun, Mechanical characterization of nanotructured tib2 coatings using microscratch techniques. tribology and interface engineering series, Elsevier Masson SAS, 2006.
[15] M. Alfreider, J. Zechner, D. Kiener, Addressing Fracture Properties of Individual Constituents Within a Cu-WTi-SiOx-Si Multilayer, JOM 72 (2020) 4551–4558.
[16] M. Alfreider, R. Bodlos, L. Romaner, D. Kiener, The influence of chemistry on the interface toughness in a WTi-Cu system, Acta. Mater. 230 (2022) 117813.
[17] D.B. Marshall, A.G. Evans, Measurement of adherence of residually stressed thin films by indentation. I. Mechanics of interface delamination, J. Appl. Phys. 56 (1984) 2632–2638.
[18] M.D. Kriese, W.W. Gerberich, N.R. Moody, Quantitative adhesion measures of multilayer films: Part II. Indentation of W/Cu, W/W, Cr/W, J. Mater. Res. 14 (1999) 3019–3026.
[19] M. Omiya, K. Kishimoto, T. Nakano, Evaluation of the interfacial strength of layered structures by indentation method, J. Appl. Mech., Trans. ASME 75 (2008) 0310061–0310066.
[20] K. Kozuki, K. Kishimoto, Film Thickness Dependency of Interfacial Strength Evaluation for Thin Film Coating Structure by Nanoindentation Method, J. Solid Mecha. Mater. Eng. 4 (2010) 771–780.
[21] K. Inoue, F. Triawan, K. Inaba, K. Kishimoto, M. Nishi, M. Sekiya, K. Sekido, A. Saitoh, Evaluation of interfacial strength of multilayer thin films polymer by nanoindentation technique, Mech. Eng. J. 6 (1) (2019), https://doi.org/10.1299/mej.18-00326.
[22] J.U. Malzbender, G.D. With, Energy dissipation, fracture toughness and the indentation load □ displacement curve of coated materials, Surf. Coat. Technol. 135 (2000) 60–68.
[23] X. Li, B. Bhushan, Measurement of fracture toughness of ultra-thin amorphous carbon films, Thin Solid Films 315 (1998) 214–221.
[24] J. Chen, S.J. Bull, Indentation fracture and toughness assessment for thin optical coatings on glass, J. Phys. D. Appl. Phys. 40 (2007) 5401–5417.
[25] P. Benjamin, C. Weaver, Measurement of adhesion of thin films, Proc. R Soc. Lond. A Math. Phys. Sci. 254 (1960) 163–176.
[26] M.T. Laugier, An energy approach to the adhesion of coatings using the scratch test, Thin Solid Films 117 (1984) 243–249.
[27] N. Deyneka-Dupriez, et al., Interfacial adhesion and friction of pyrolytic carbon thin films on silicon substrates, J. Mater. Res. 23 (2008) 2749–2756.
[28] X. Boddaert, et al., Organic ultrathin film adhesion on compliant substrate using scratch test technique, Thin Solid Films 528 (2013) 194–198.
[29] M. Humood, et al., Nanoindentation and nanoscratch of sub-micron polymer nanocomposite films on compliant substrate, Thin Solid Films 736 (2021).
[30] Y. Hang, G. Liu, K. Huang, W. Jin, Mechanical properties and interfacial adhesion of composite membranes probed by in-situ nano-indentation/scratch technique, J. Memb. Sci. 494 (2015) 205–215.
[31] S.Y. Chang, H.C. Tsai, J.Y. Chang, S.J. Lin, Y.S. Chang, Analyses of interface adhesion between porous SiOCH low-k film and SiCN layers by nanoindentation and nanoscratch tests, Thin Solid Films 516 (2008) 5334–5338.
[32] J. Den Toonder, J. Malzbender, G. De With, R. Balkenende, Fracture toughness and adhesion energy of sol-gel coatings on glass, J. Mater. Res. 17 (2002) 224–233.
[33] S. Lafaye, M. Troyon, On the friction behaviour in nanoscratch testing, Wear 261 (2006) 905–913.
[34] S. Zak, C.O.W. Trost, P. Kreiml, M.J. Cordill, Accurate measurement of thin film mechanical properties using nanoindentation, J. Mater. Res. 37 (2022) 1373–1389.
[35] C.C. Zhu, et al., The dynamical mechanical properties of tungsten under compression at working temperature range of divertors, J. Nucl. Mater. 469 (2016) 120–124.
[36] C. Ren, et al., Methods for improving ductility of tungsten - A review, Int. J. Refract. Metals Hard Mater. 75 (2018) 170–183.
[37] R.W. Armstrong, W.L. Elban, S.M. Walley, Nano-Indentation Hardness and Strain Hardening of Silicon, Sodium Chloride and Tungsten Crystals, Exp. Mech. 62 (2022) 359–364.
[38] R. Saha, W.D. Nix, Effects of the substrate on the determination of thin film mechanical properties by nanoindentation, Acta. Mater. 50 (2002) 23–38.
[39] M.P. De Boer, W.W. Gerberich, Microwedge indentation of the thin film fine line – II. Experiment, Acta Mater 44 (1996) 3177–3187.
[40] B.S. Lakshmi Prasad, A. Raja Annamalai, Effect of Rhenium addition on tungsten heavy alloys processed through spark plasma sintering, Ain. Shams. Eng. J. 12 (2021) 2957–2963.
[41] T.Y. Tsui, G.M. Pharr, Substrate effects on nanoindentation mechanical property measurement of soft films on hard substrates, J. Mater. Res. 14 (1999) 292–301.
[42] X. Xiao, et al., High temperature nano-indentation of tungsten: Modelling and experimental validation, Mater. Sci. Eng. A 743 (2019) 106–113.
[43] R. Hertzberg, Deformation and Fracture Mechanics of Engineering Materials, John Wiley & Sons Inc, Hoboken, New Jersey, 2013.
[44] S.J. Bull, Microstructure and indentation response of TiN coatings: The effect of measurement method, Thin Solid Films 688 (2019) 137452.
[45] W.C. Oliver, G.M. Pharr, An improved technique for determining hardness and elastic modulus using load and displacement sensing indentation experiments, J. Mater. Res. 7 (1992) 1564–1583.
[46] A. Kleinbichler, et al., New Insights into Nanoindentation-Based Adhesion Testing, JOM 69 (2017) 2237–2245.
[47] A. Lassnig, et al., Microstructural Effects on the Interfacial Adhesion of Nanometer-Thick Cu Films on Glass Substrates: Implications for Microelectronic Devices, ACS Appl. Nano. Mater. 4 (2021) 61–70.
[48] M.P. De Boer, M. Kriese, W.W. Gerberich, Investigation of a new fracture mechanics specimen for thin film adhesion measurement, J. Mater. Res. 12 (1997) 2673–2685.
[49] A. He, H. Huang, Nanoscratch characteristics and interfacial adhesion energy of SiN/GaAs film/substrate bilayer systems, Int. J. Surf. Sci. Eng. 7 (2013) 382–396.
[50] S.J. Bull, Failure mode maps in the thin film scratch adhesion test, Tribol. Int. 30 (1997) 491–498.
[51] P.A. Steinmann, Y. Tardy, H.E. Hintermann, Adhesion testing by the scratch test method: The influence of intrinsic and extrinsic parameters on the critical load, Thin Solid Films 154 (1987) 333–349.
[52] S. Wirasate, F.J. Boerio, Effect of Adhesion , Film Thickness , and Substrate Hardness on the Scratch Behavior of Poly (carbonate) Films, J. Adhes. 8464 (2005) 509–528.
[53] P.J. Burnett, D.S. Rickerby, The Scratch Adhesion Test: An Elastic-Plastic Indentation Analysis, Thin Solid Films 157 (1988) 233–254.
[54] W. Wang, et al., Experimental and numerical investigation on the effect of scratch direction on material removal and friction characteristic in BK7 scratching, Materials 13 (2020).